Bioactive Materials 43 (2025) 460–470

Contents lists available at ScienceDirect

Bioactive Materials

journal homepage: www.keaipublishing.com/en/journals/bioactive-materials

Readily constructed squaraine J-aggregates with an 86.0 % photothermal conversion efficiency for photothermal therapy

Xin Xie [a,1], Yafang Dong [c,1], Yuan Zhang [e,1], Zongliang Xie [b], Xinsheng Peng [a], Yong Huang [a], Wei Yang [f], Bowen Li [b,**], Qiqing Zhang [a,d,*]

[a] School of Pharmacy, Guangdong Medical University, Dongguan, 523808, China
[b] Department of Chemical and Biomolecular Engineering, National University of Singapore, 5A Engineering Drive 1, 117411, Singapore
[c] Shenzhen People's Hospital, The First Affiliated Hospital, Southern University of Science and Technology, Shenzhen, Guangdong, 518020, China
[d] Institute of Biomedical Engineering, Chinese Academy of Medical Sciences and Peking Union Medical College, Tianjin, 300192, China
[e] Fujian Bote Biotechnology Co. Ltd, Fuzhou, Fujian, China
[f] Department of Critical Care Medicine, Longgang Central Hospital, Shenzhen 6082 longgang Road, Shenzhen, 518116, Guangdong, China

ARTICLE INFO

Keywords:
Photothermal conversion efficiency
Long absorption wavelengths
Squaraine
J-aggregation
Photothermal therapy

ABSTRACT

The development of photothermal agents with high photothermal conversion efficiency (PCE) and long absorption wavelengths is crucial for safe and effective anti-cancer treatment. However, achieving these advantages often requires precise molecular design and complex synthetic procedures. In this study, we present a simple, precise, and effective method for fabricating photothermal agents with high PCE using long wavelength excitation. This approach involves linking two electron-donating components, diphenylamine (DPA), and an electron-withdrawing squaraine (SQ), via a π-bridge thiophene (T). The resulting D-π-A-π-D structure leads to a red-shifted absorption band. Within the DTS structure, DPA functions as a molecular rotor, T serves as a coplanar backbone, and SQ promotes J aggregation. When DTS nanoparticles (NPs) are fabricated using an amphiphilic nano-carrier, the maximum absorption wavelength shifts from 701 to 803 nm. This shift is accompanied by reduced fluorescence and an exceptionally high PCE of 86.0 %. Both in vitro and in vivo assessments confirm that DTS NPs exhibit strong potential for photothermal antitumor therapy. Overall, this strategy offers a valuable framework for designing photothermal agents with clinical applications in mind, offering a simpler and more efficient approach to achieving high PCE and long absorption wavelengths.

1. Introduction

Photothermal therapy (PTT) has emerged as a non-invasive, high-efficiency and biosafe cancer treatment strategy that utilizes photothermal agents (PTAs) to convert light energy into heat, efficiently killing cancer cells [1–6]. Importantly, this therapeutic approach is particularly beneficial for combating cancers that have developed multi-drug resistance (MDR) to traditional chemotherapeutics [7–9]. Currently, extensive research efforts are focused on exploring photothermal agents, with organic photothermal agents standing out due to their desirable biocompatibility, biodegradability, and ease of acquisition and modification, making them promising candidates for clinical applications [10–12]. However, traditional photothermal process require stronger irradiation using short wavelengths for prolonged time, which presents significant challenges such as limited tissue penetration and suboptimal photothermal conversion efficiency (PCE), thereby hindering the widespread application of PTT [13,14]. To address these challenges, there is a need for photothermal agents with longer near-infrared absorption wavelengths and higher PCE. Achieving this typically involves precise design and complex synthesis of photothermal agents, which can be time-consuming and costly [15]. Therefore, there is an urgent need to develop a simple and efficient strategy to synthesize organic PTAs to overcome these challenges.

To address these issues, there is increasing interest in synthesizing

Peer review under responsibility of KeAi Communications Co., Ltd.
* Corresponding author. School of Pharmacy, Guangdong Medical University, Dongguan, 523808, China.
** Corresponding author.
E-mail addresses: bowen_86@nus.edu.sg (B. Li), zhangqiq@126.com (Q. Zhang).
[1] The authors contributed equally to this work.

https://doi.org/10.1016/j.bioactmat.2024.09.031
Received 7 July 2024; Received in revised form 9 September 2024; Accepted 22 September 2024
Available online 10 October 2024

photothermal agents with high PCE by modulating relaxation pathways during the photochemical process [16–18]. Generally, light energy absorbed by chromophores dissipates through two main relaxation pathways: nonradiative decay and radiative decay, with heat generation depending on non-radiative decay [19–21]. Theoretical insights suggest that suppressing radiative decay channels or promoting the nonradiative decay pathway results in exclusive photothermal conversion. Previous studies have demonstrated that robust π-π interactions, arising from the coplanar structure of organic dyes, can quench fluorescence and indirectly boost photothermal properties by inhibiting radiative dissipation [22–25]. Another frequently employed strategy involves introducing molecular rotors to activate intermolecular motion, facilitating efficient dissipation of non-radiative energy and maximizing light-to-heat conversion [26–29]. However, planar structures with molecular rotors often lead to H-aggregation in the aggregated state, which hampers photothermal performance by restricting molecular rotation and causing a blue shift in the absorption wavelength [30,31]. To achieve a longer near-infrared (NIR) absorption wavelength, primary strategies involve expanding the π-conjugate structure or constructing a donor-acceptor structure [32–36]. However, this approach requires meticulous molecular manipulation, limiting the development of longer wavelength dyes.

In response to these requirements, J-aggregation emerges as a promising phenomenon characterized by a "slip-stack" arrangement of individual molecules in a head-to-tail manner. This arrangement induces a significant redshift in absorption, facilitating long wavelength photothermal therapy without altering molecular structure and energy levels [37–39]. This phenomenon provides a straightforward and effective strategy for designing PTAs as candidates for tumor treatment. To date, only a few specific chromophores exhibit J-aggregation behavior, including perylenediimide [40,41], chlorophyll [42,43], cyanine [44–46], boron dipyrromethene (BODIPY) [47–50], and squaraine (SQ) [51,52]. Among these, SQ distinguishes itself due to its unique rigidity, planar structure and zwitterionic characteristic, resulting in strong absorption in NIR region. Furthermore, SQ exhibits advantages such as a high molar extinction coefficient, good photothermal stability, and low toxicity, making it a suitable candidate for constructing PTAs [53–55].

In this study, we propose a straightforward strategy to develop highly efficient and safe PTT agents for anti-cancer treatment. The PTT agent (DTS) was designed with specific molecular components to enhance absorption wavelength and boost its PCE. As illustrated in Scheme 1, DTS comprises two strong electron-donating diphenylamine (DPA) units, a typical electron-withdrawing squaraine (SQ) core, and two thiophene (T) linkers. In this molecular architecture, the DPA moiety acts as a strong electron donor and molecular rotor, while the SQ core serves as an acceptor, and the thiophene functions as a π bridge with a coplanar structure. The D-π-A-π-D pattern of conjugated small molecules in DTS promotes extensive electron delocalization and redshifts absorption, facilitating non-radiative decay pathways and suppressing radiative decay pathways. To fabricate DTS nanoparticles (NPs)

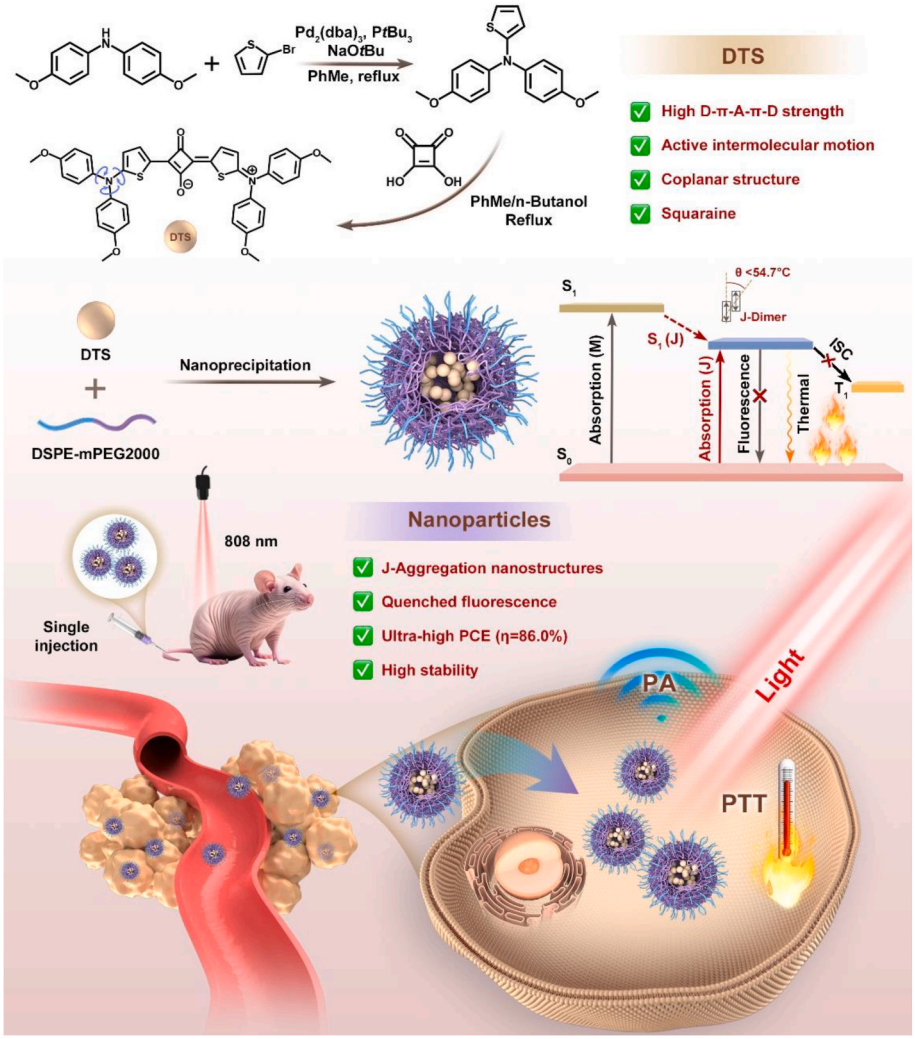

Scheme 1. Schematic illustration of molecular structures of DTS, nanofabrication and the application of PA imaging-guided photothermal therapy.

suitable for in vivo applications, we utilized an amphiphilic polymer, 1,2-distearoyl-sn-glycero-3-phosphoethanolamine-N-[maleimide(poly-ethylene glycol)-2000] (DSPE-PEG2000). This DSPE-PEG2000 ensures favorable stability and biocompatibility of the resulting DTS NPs. Additionally, the SQ-mediated J-aggregation behavior further enhances the redshift effect of DTS NPs, and thus DTS NPs exhibited excellent photothermal conversion capacity, achieving an impressive PCE of 86.0 % under an 808 nm laser. Moreover, they demonstrated remarkable stability and efficient antitumor performance both in vitro and in vivo. Our strategy provides novel insights into constructing squaraine-based PTT agents with extended absorption wavelengths and ultra-high PCE, offering a high-efficiency and safe approach for anti-cancer therapy.

2. Results and discussion

The synthesis of DTS involved a straightforward two-step process, as illustrated in Scheme 1. Initially, an intermediate product was obtained through a Buchwald–Hartwig cross-coupling reaction between diarylamine and 2-bromothiophene. Subsequently, the final product was prepared via a simple condensation reaction with squaric acid. The structure of DTS (Fig. 1A) was confirmed using nuclear magnetic resonance (NMR) and high-resolution mass spectrometry (HR-MS) (Figs. S1–S3). Time-dependent density-functional theory (TD-DFT) calculations at B3LYP/6–311g(d) level were performed to understand the photophysical properties of DTS [56,57]. Fig. 1B revealed that the electron cloud of the highest occupied molecular orbital (HOMO) of DTS extends across the entire conjugated skeletons, while the lowest unoccupied molecular orbital (LUMO) is dominantly located on the core of electron-deficient acceptor (SQ). This distribution signified a pronounced donor-acceptor (D-A) interaction, contributing to the molecule's extended absorption. The optical properties of DTS were further measured. Firstly, we measured the changes of absorption spectra of DTS in THF/water binary solvents with different water fraction (f_w). As can be seen from Fig. S4, when the water fraction reached 80 %, a significant redshift in the absorption wavelength was observed, suggesting the formation of J-aggregates. Then, the UV–vis–NIR spectra of DTS in tetrahydrofuran (THF) solution or solid states were also characterized (Fig. 1C). It was observed that DTS exhibited a maximum absorption

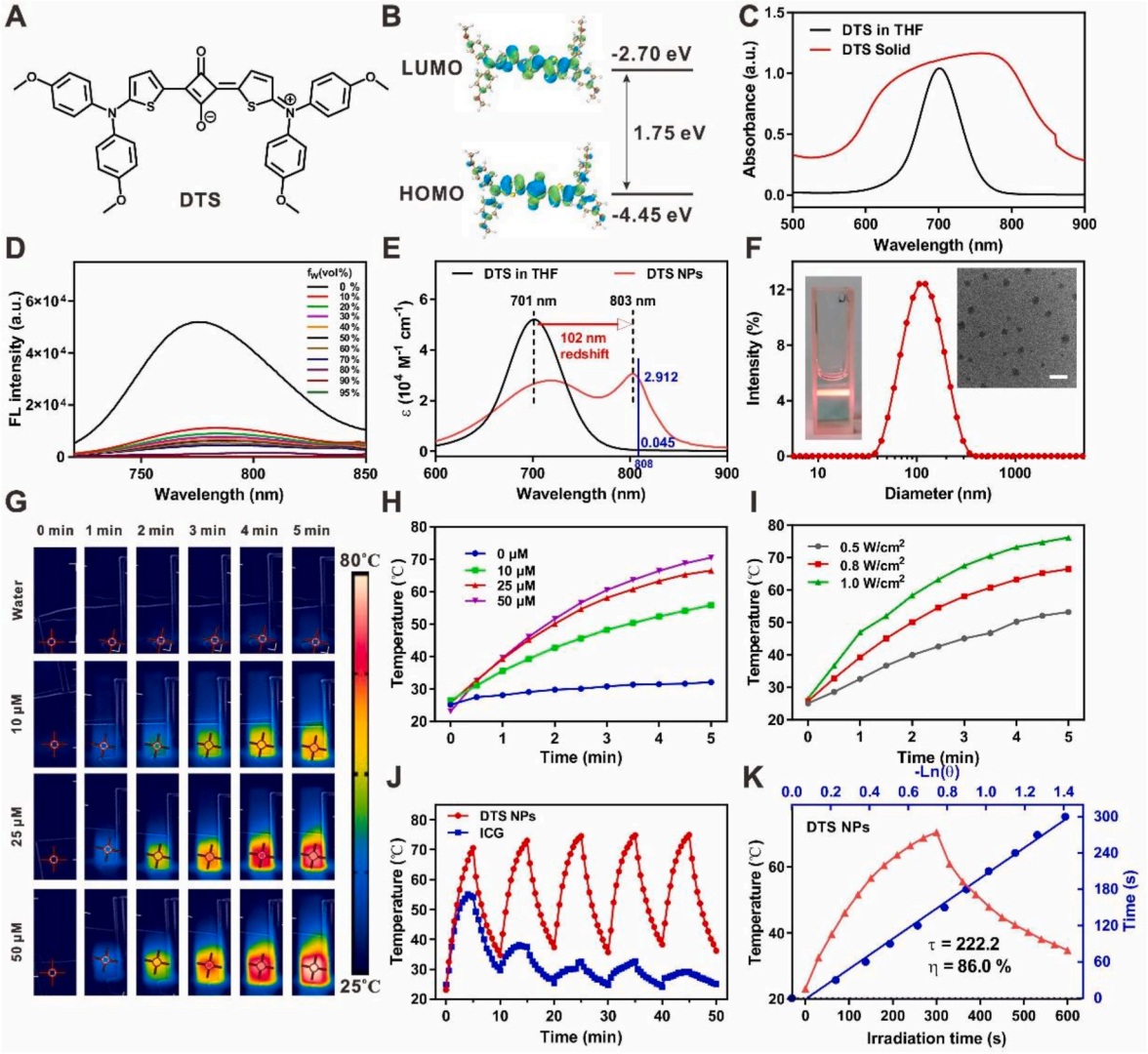

Fig. 1. A) The chemical structure of DTS. B) calculated LOMOs and HUMOs of DTS. C) The absorption spectra of DTS solution in THF and DTS solid. D) The fluorescence emission spectra of DTS in THF/water binary solvents with different water fraction (f_w). E) The absorption spectra of DTS solution in THF and DTS NPs. F) The size distribution of DTS NPs determined by DLS. Inset: Tyndall phenomenon and TEM image. Scale bar: 200 nm. G) IR thermal images and H) Photothermal curves of DTS NPs with different concentrations under 808 nm laser irradiation (0.8 W/cm^2, 5 min). I) Photothermal curves of DTS NPs under 808 nm laser irradiation at different power densities (0.5, 0.8, 1.0 W/cm^2) for 5 min. J) Photothermal stability of DTS NPs and ICG in aqueous solution during five on/off irradiation cycles. K) Calculated photothermal conversion efficiency of DTS NPs. τ is the associated time constant.

peak at 701 nm in THF solution, while in the solid state, DTS displayed a broadened absorption spectrum accompanied by J-aggregation, characted with red-shifted absorption. To investigate the impact of J-aggregation behavior of DTS on photoluminescence (PL) properties, we recorded the fluorescence variation in THF/water with different water fractions (f_w). Fig. 1D illustrated that the fluorescence emission intensity significantly decreased with the increase of f_w at 680 nm wavelength excitation. When $f_w = 95$ vol %, the fluorescence emission is completely quenched. While there is no fluorescence was observed in THF/water with different water fractions under 808 nm excitation (Fig. S5). These results indicated that the J-aggregation behavior of DTS greatly inhibited radiative decay pathway, potentially enhancing photothermal effects through nonradiative energy dissipation.

Given the in vivo application of DTS and the advantage of its J-aggregation, we constructed DTS NPs by encapsulating them with DSPE-PEG_{2000} using a nanoprecipitation method. As expected, DTS NPs exhibited an obvious redshift behavior, with the maximum absorption wavelength redshift by 102 nm (from 701 to 803 nm) following the preparation of the nanomaterial (Fig. 1E). Moreover, the molar absorption coefficients (ε) of DTS, either dissolved in THF or formulated into nanoparticles, was calculated to be 0.045 and 2.912×10^4 M^{-1} cm^{-1} at 808 nm, respectively, indicating their efficient light-capturing capacity at 808 nm. We characterized the particle size and morphology of the prepared DTS NPs using dynamic light scattering (DLS) and transmission electron microscopy (TEM). As depicted in Fig. 1F, the DLS result showed that DTS NPs exhibited a suitable average particle size and narrow particle size distribution (Z-average = 124.3 nm, PDI = 0.137). While TEM images displayed that DTS NPs possessed regular spherical structure, with a diameter slightly smaller than that measured by DLS, which could be explained by the hydration layer of nanoparticles. Meanwhile, the zeta potential of DTS NPs was measured to be −10.5 mV (Fig. S6). Additionally, after one week of storage, no significant changes in particle size and PDI were observed, indicating good colloidal stability (Fig. S7). Besides, we co-incubated DTS NPs (10 μM) with 1 mM GSH, Cys and Hcy for 24 h, and then studied the changes in particle size, absorption spectra, and photothermal properties. As shown in Fig. S8, there is no obvious difference in average diameter, absorption spectra, and photothermal properties, which indicated that DTS NPs exhibits significant stability in the presence of various biothiols.

To evaluate the photothermal properties of DTS NPs, we examined its temperature elevations at different concentrations (0, 10, 25, and 50 μM) and laser intensities (0.5, 0.8, and 1.0 W/cm^2) using an IR thermal imaging system. As shown in Fig. 1G and H, the temperature of DTS NPs (25 μM) rapidly rose from 25.8 °C to 66.5 °C within 5 min of 808 nm laser irradiation (0.8 W/cm^2), whereas the negative group (water) exhibited negligible temperature changes. Furthermore, DTS NPs displayed temperature changes that were dependent on concentration and laser intensity (Fig. 1I). The elevated temperature of DTS NPs irradiated with 0.8 W/cm^2 laser for 5 min could provide sufficient heat for subsequent in vitro and in vivo treatments. Additionally, the relatively low laser intensity minimizes the potential impact on normal cells and tissues. Therefore, the laser power was set to 0.8 W/cm^2 for the following experiments. Subsequently, the photothermal behavior and thermal stability of DTS NPs and ICG during the repeated heating/cooling cycles was also evaluated, as shown in Fig. 1J. The DTS NPs solution maintained a stable temperature of over 70 °C even after five heating and cooling cycles, whereas the photothermal performance of ICG sharply decreased after just one cycle. Based on the temperature change profiles, the PCE value of DTS NPs was calculated to be 86.0 %, surpassing the majority of reported organic PTAs (Fig. 1K). We also determined the PCE of DTS solution (in DMF) under the 808 nm laser irradiation (Fig. S9). This result revealed that both the degree of temperature change and the PCE of DTS NPs are considerably higher than that of DTS solution, suggesting that nanoparticle construction mediated J-aggregation not only increased the molar absorption coefficient of DTS at the wavelength of 808 nm but also enhanced its PCE. To evaluate the ISC process of DTS NPs, the dichloro-dihydro-fluorescein (DCFH) was employed as the total ROS indicator. The ability of DTS NPs to produce ROS was investigated by comparing it with FDA-approved indocyanine green (ICG). As shown in Fig. S10, DTS NPs exhibited a significantly reduced capacity for the generation of ROS compared to ICG, while ICG was commonly used as an imaging agent and photothermal agent due to its lower $^1O_2$ quantum yield (approximately 0.2 %) [58,59], indicating the inhibition of ISC decay pathway. Further photostability tests (Fig. S11) showed that DTS NPs exhibited only a slight reduction in absorption after 30 min of 808 nm laser irradiation, while ICG suffered severe photobleaching, as evidenced by the change in solution color post-irradiation. Taken together, these results demonstrated that DTS NPs possessed the ultra-high photothermal conversion efficiency, low ROS generation, quenched fluorescence, and exceptional photothermal stability, making them a potential promising photothermal reagent for cancer treatment.

The superior photothermal properties of DTS NPs, including their extended NIR absorption wavelength and ultra-high PCE, encouraged us to gain an in-depth understanding of the photothermal mechanism. The molecular packing mode in solid state was evaluated by analyzing single-crystal structure of DTS. The DTS single crystal, grown from a dichloromethane (DCM)/n-hexane (v/v = 1:2) solution, was subjected to single-crystal X-ray diffraction (XRD) analysis (Fig. 2A and Table S1). The DTS single crystal demonstrated a monoclinic structure. As illustrated in Fig. 2D, DTS exhibited a relatively planar molecular conformation with a minimal torsion angle of 7.35° between the squaraine (SQ) core and the thiophene (T), facilitating strong intermolecular interactions that quench the emission in the aggregate state and enhance the non-radiative transitions. Notably, the single-crystal structure also shown that DTS exhibited a head-to-tail arrangement with a slipping angle of 30.92°, smaller than the critical angle of 54.7° required for J-aggregation [60], and the distance between adjacent DTS was approximately 3.115 Å (Fig. 2B).The planar structure formed by squaraine and thiophene favors aggregation, while the electron donor methoxydiphenylamine introduces significant steric hindrance and non-planarity, resulting in a head-to-tail arrangement (J-aggregation).

Subsequently, TD-DFT calculations were conducted to elucidate the redshift phenomenon. We defined the dispersed molecular state of DTS as the monomer, while the aggregated state was defined as J-dimer and J-trimer, respectively, based on the degree of aggregation. As shown in Fig. 2C, with the occurrence of aggregation, the energy gap of S1 (excited-state)-S0 (ground-state) gradually decreased, consistent with the redshift phenomenon of aggregated DTS. According to the energy band gap theory, a reduced energy band gap typically accelerates non-radiative decay processes, thereby weakening fluorescence [61–63]. Indeed, the experimental results of the fluorescence quenching in Fig. S12 further validate the theoretical calculations. Moreover, DFT calculations were performed to understand ISC process resulted by J-aggregates. As displayed in Fig. 2C, the formation of J-type trimer reduced the ΔE_{st} compared to the monomer (from 1.26 to 0.82 eV). However, typically, ISC process will be favorably triggered when the ΔE_{st} below 0.3 eV [64,65]. This result further corroborated the experimental results for the detection of ROS. These results indicated that photothermal become the dominant decay pathway, leading to the generation of exclusive photothermal effects due to the suppression of radiative decay pathways (for fluorescence) and ISC process (for ROS). Furthermore, the geometric configuration of DTS changes significantly after excitation, with large root-mean-square displacement (RMSD) values of 0.72 Å, providing a heat generation channel for energy dissipation. In general, the theoretical calculation results analyzed the molecular packing mode of DTS crystals, revealed the mechanism of its redshift phenomenon and ultra-high PCE, and provided a theoretical foundation for the future design of photothermal molecules.

Inspired by the superior photothermal properties of DTS NPs, we further investigated their cytotoxicity against different cancer cells (4T1, CT26, and HepG2) using CCK-8 assay. In all cancer cells, DTS NPs,

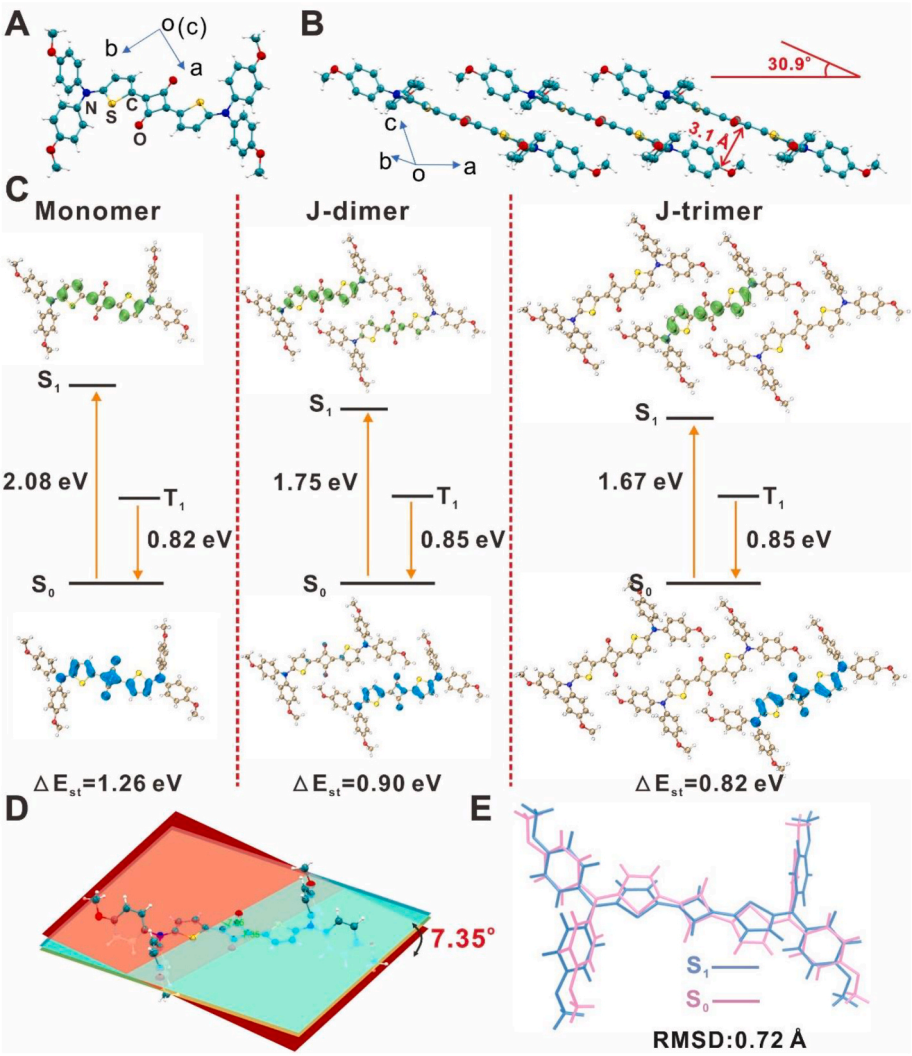

Fig. 2. A) X-ray single crystal structure of DTS. H atoms are omitted for clarity. B) molecular packing diagrams of DTS in the crystalline state. C) Calculated molecular orbitals of monomer, J-dimer and J-trimer and their orbital energies in the optimized excited state based on TD-DFT method. D) Optimized ground-state (S0) geometry of DTS. E) The RMSD of optimized ground-state (S0) and excited-state (S1) geometry.

even at the high concentration of 40 μM, exhibited negligible cytotoxicity in the absence of laser exposure (Fig. 3A–C). Upon exposure to an 808 nm laser (0.8 W/cm^2) for 5 min, the cytotoxicity of DTS NPs sharply increased with concentration. Quantitatively, the cell viability of DTS NPs (40 μM) with laser irradiation toward 4T1, CT26 and HepG2 were reduced to be 4.3 %, 5.8 %, and 2.0 %, respectively. Subsequently, the cell death of DTS NPs was also visualize by a calcein-AM/PI staining experiment (live cells: green; dead cells: red). As anticipated, the cells treated with DTS NPs + laser (0.8 W/cm^2, 5 min) showed bright red fluorescence, while cells treated with other formulations displayed only green fluorescence, indicating the effective cancer cell-killing capability of the photothermal effect of DTS NPs (Fig. 3D). Furthermore, the apoptosis pathway under photothermal effect was also evaluated by FITC/PI double staining assay. Compared to the total apoptosis rate of less than 10 % in other groups, the apoptosis rate in DTS NPs + laser group significantly increased to 73.5 % (Fig. 3E). Collectively, these results suggested that DTS NPs exhibited good biocompatibility without laser irradiation and efficient photothermal therapy effect in cancer cells.

The exciting in vitro results of DTS NPs led us to explore their application in 4T1 tumor-bearing mice. Initially, we assessed the biological distribution of DTS NPs in vivo to evaluate their drug accumulation in tumor regions. Multimode imaging offers more precise guidance for the biological distribution of nanomaterials. Given that the quenched fluorescence of DTS NPs themselves was not suitable as a fluorescence imaging contrast agent, the commercial dye DiR and DTS were co-loaded into DSPE-PEG2000 to construct DiR-loaded DTS NPs (Fig. S13). Fluorescence imaging of mice was recorded at different times after intravenous injection of DiR-loaded DTS NPs. As depicted in Fig. 4A and B, the fluorescence intensity of the tumor area gradually increased with prolonged time and reached its maximum value at 8 h post-injection. After 24 h post-injection, the main organs and tumor tissues were harvested, and ex vivo fluorescence images and average fluorescence intensity were analyzed in Fig. S14. The fluorescence intensity in tumor tissue was significantly higher than that in main organs. These results demonstrated that DiR-loaded DTS NPs effectively accumulate at the tumor area benefiting from the EPR effect.

Given their exceptional photothermal effect, DTS NPs can serve as an exogenous photoacoustic (PA) contrast agent. From the photoacoustic images and quantitative data of tumor tissue (Fig. 4C and D), it can be observed that the changes in photoacoustic signal and fluorescence signal intensity exhibited similar trends over time. Specifically, both signals reached their maximum values at 8 h post-injection, providing the optimal irradiation time point for subsequent photothermal therapy. Then, photothermal imaging experiments in mice were performed to further evaluate the in vivo photothermal performance using an IR

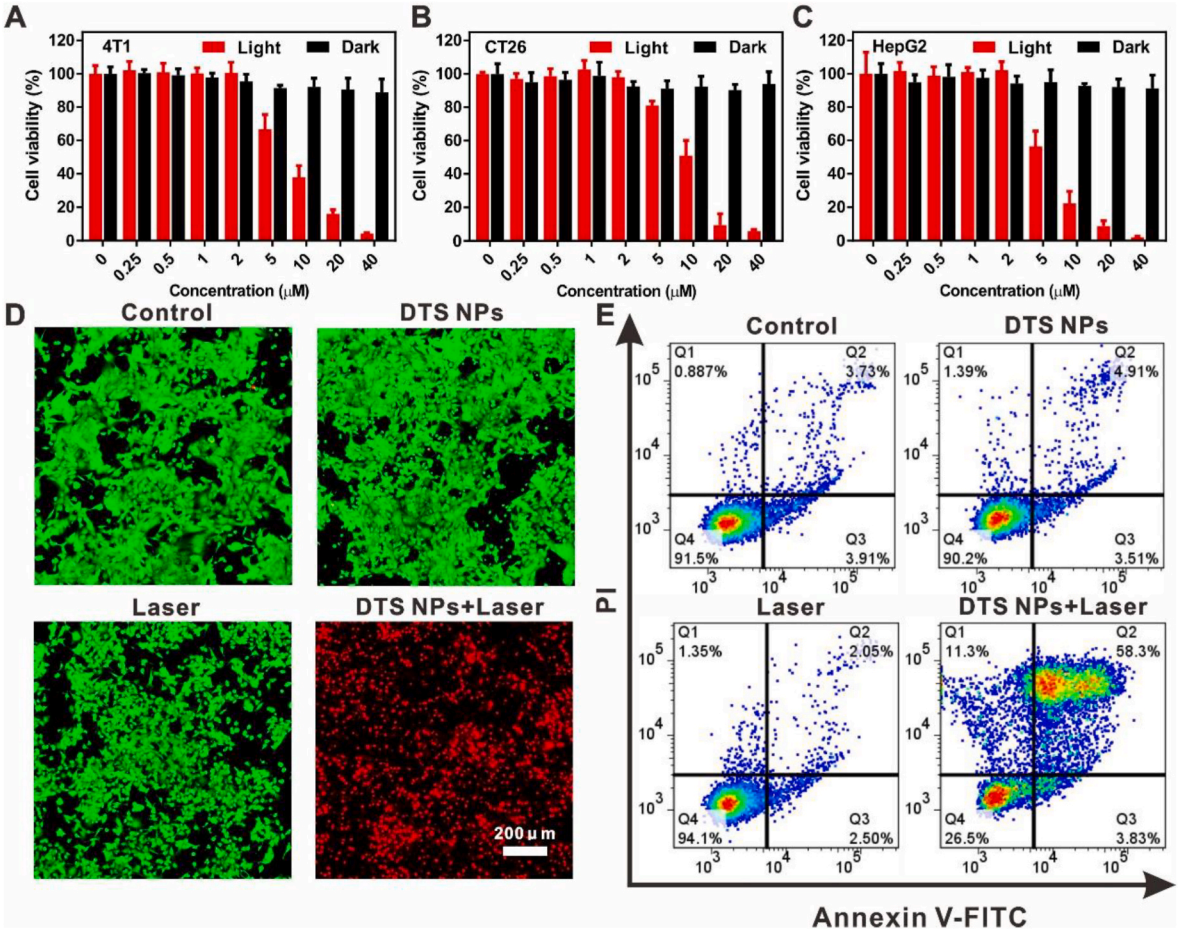

Fig. 3. Cell viability of A) 4T1, B) CT26, and C) HepG2 cells incubated with DTS NPs at different concentrations with or without 808 nm light irradiation (0.8 W/cm^2, 5 min). D) Live/dead imaging of 4T1 cells stained with Calcein-AM (green) and PI (red) upon treatment with different formulation. E) Flow cytometry analysis using Annexin V-FITC/PI dual staining for 4T1 cells upon treatment with different formulation.

thermal camera. We injected PBS and DTS NPs into mice by tail vein and irradiated the tumor tissue with 808 nm laser (0.8 W/cm^2) for 10 min at 8 h post-injection, then recorded the temperature changes in the tumor region (Fig. 4E and F). The temperature at the tumor location in mice treated with DTS NPs gradually increased and stabilized at around 53 °C, sufficient to ablate the tumor cells [66–68]. In contrast, mice treated with PBS exhibited only a slight temperature elevation. These results clearly indicated that DTS NPs can be used as a potential photothermal agent for tumor therapy.

Motivated by the efficient tumor accumulation and superior photothermal properties, we evaluated the in vivo antitumor efficacy in 4T1 tumor-bearing mice. When the tumor volume reached approximately 100 mm^3, the mice were randomly assigned into four groups (n = 5) and treated with (1) PBS, (2) PBS + laser, (3) DTS NPs, and (4) DTS NPs + laser. The administration was carried out only once, and the laser irradiation (808 nm, 0.8 W/cm^2) was performed for 10 min at 8 h after the injection. The tumor volume and body weight were recorded every other day during the 18 days period. As shown in Fig. 5A–C, the relative tumor volume in groups treated with PBS, PBS + laser and DTS NPs exhibited uncontrollable and rapid growth. Remarkably, tumors in mice treated with DTS NPs + laser were essentially completely ablated at day 6, with no recurrence observed in subsequent observations, indicating excellent therapeutic efficiency of the photothermal effect of DTS NPs in vivo. To further evaluate the mechanism of in vivo anti-cancer therapy, histochemical and immunohistochemical analyses were investigated by hematoxylin and eosin (H&E), terminal deoxynucleotidyl transferase dUTP nick end labeling (TUNEL) and Ki67 staining of tumor sections. The TUNEL assay works by labeling the ends of fragmented DNA strands in cells. The enzyme terminal deoxynucleotidyl transferase (TdT) adds labeled nucleotides (dUTP) to the breaks in DNA, which can then be visualized using fluorescence microscopy or other methods. It is used to detect DNA fragmentation, which is a hallmark of apoptosis. Ki67 staining involves using antibodies to detect the Ki67 protein in cells. The presence of Ki67 indicates cells are in active phases of the cell cycle (G1, S, G2, or mitosis), while its absence indicates cells in the resting phase (G0). Ki67 is a protein that is associated with cell proliferation. Among them, the tumors in group DTS NPs + laser were removed on day 1 post-treatment, when the tumors were not yet eliminated completely. While the tumors in the other groups were harvested on day 18. As evident from Fig. 5E, DTS NPs + laser group showed the worst severe apoptosis and necrosis (H&E and TUNEL staining), as well as the least proliferation of cancer cells (Ki67 staining) compared to other groups. Moreover, throughout the treatment, no significant loss was observed in any of the mice (Fig. 5D), indicating satisfactory biocompatibility of DTS NPs in vivo. Furthermore, H&E staining images of major organs further confirmed the biosafety of DTS NPs (Fig. S15). These results collectively suggest that DTS NPs exhibit effective tumor inhibition, good biocompatibility, and biosafety, making them a promising photothermal agent for cancer therapy.

3. Conclusion

In summary, we have developed a convenient and straightforward strategy to produce near-infrared (NIR)-absorbing and ultra-high

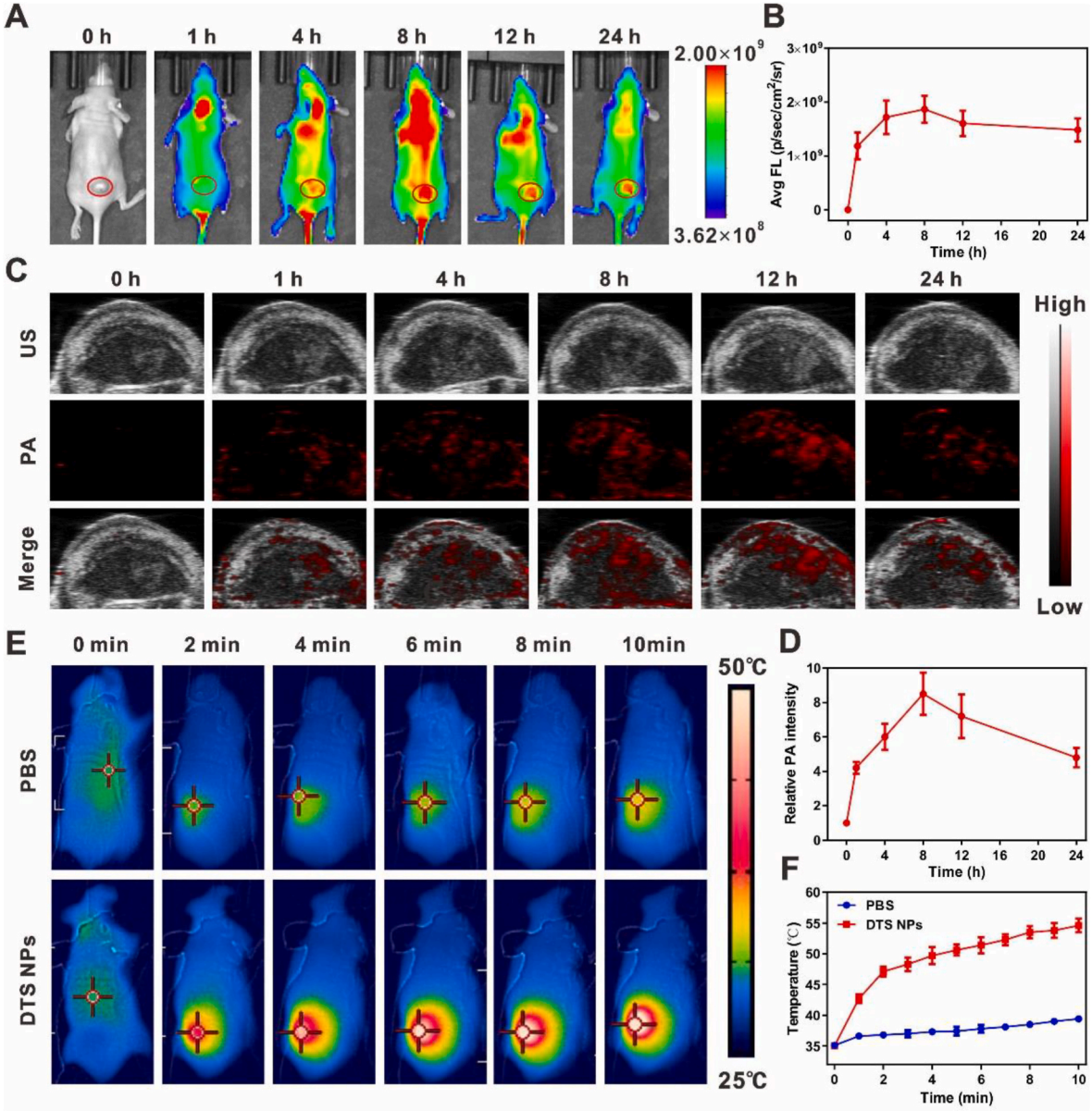

Fig. 4. A) In vivo fluorescence images of 4T1 tumor-bearing mice after intravenous injection of DiR-loaded DTS NPs at a predetermined time. The tumor region was highlighted with red circle. B) The average fluorescence intensities of tumor regions in (A). C) In vivo PA images of 4T1 tumor-bearing mice after intravenous injection of DTS NPs at a predetermined time. D) Relative PA intensity of tumor regions corresponding to (C). E) Infrared thermal images and F) temperature change curves of 4T1 tumor-bearing mice at 8 h postinjection of DTS NPs under 808 nm laser irradiation (0.8 W/cm^2) for 10 min.

photothermal conversion efficiency (PCE) PTAs nanodrug for efficient photothermal therapy. The synthesized DTS, obtained via a two-step method, incorporates diphenylamine, thiophene, and squaraine components. The D-π-A-π-D molecular structure, along with the presence of a flexible molecular rotor and squaraine-mediated J-aggregation, contributes to the remarkable properties of the resulting DTS NPs. Under 808 nm laser irradiation, the DTS NPs exhibit an outstanding PCE of 86.0 %. The underlying mechanism behind this behavior has been elucidated through detailed theoretical studies. Both in vitro and in vivo experiments have robustly confirmed the excellent photothermal stability, biocompatibility, and ultra-high photothermal conversion efficiency of DTS NPs, resulting in effective anti-tumor effects. This successful demonstration of designing a simple synthetic photothermal reagent with ultra-high PCE provides valuable insights for the development of potential clinical photothermal agents.

4. Experimental section

4.1. Computational methods

Time-dependent density-functional theory (TD-DFT) calculations at B3LYP/6–311g(d) level were performed in Gaussian 16 program, followed by the analyzing with Multiwfn software. Hirshfeld surface analyses base the single crystal were conducted with the Multiwfn software [69,70].

4.2. Procedure for the synthesis of DTS

N,N-bis(4-methoxyphenyl)thiophen-2-amine (**S1**) was synthesized according to the reported lecture with quantitative yield [71]. S1 (0.312 g, 1.0 mmol, 2.0 eq) and squaric acid (0.057 g, 0.5 mmol, 1.0 eq) were added into a 50 mL two-necked round-bottom flask with magnetic stirrer and a reflux condenser. The flask was degassed and flushed with

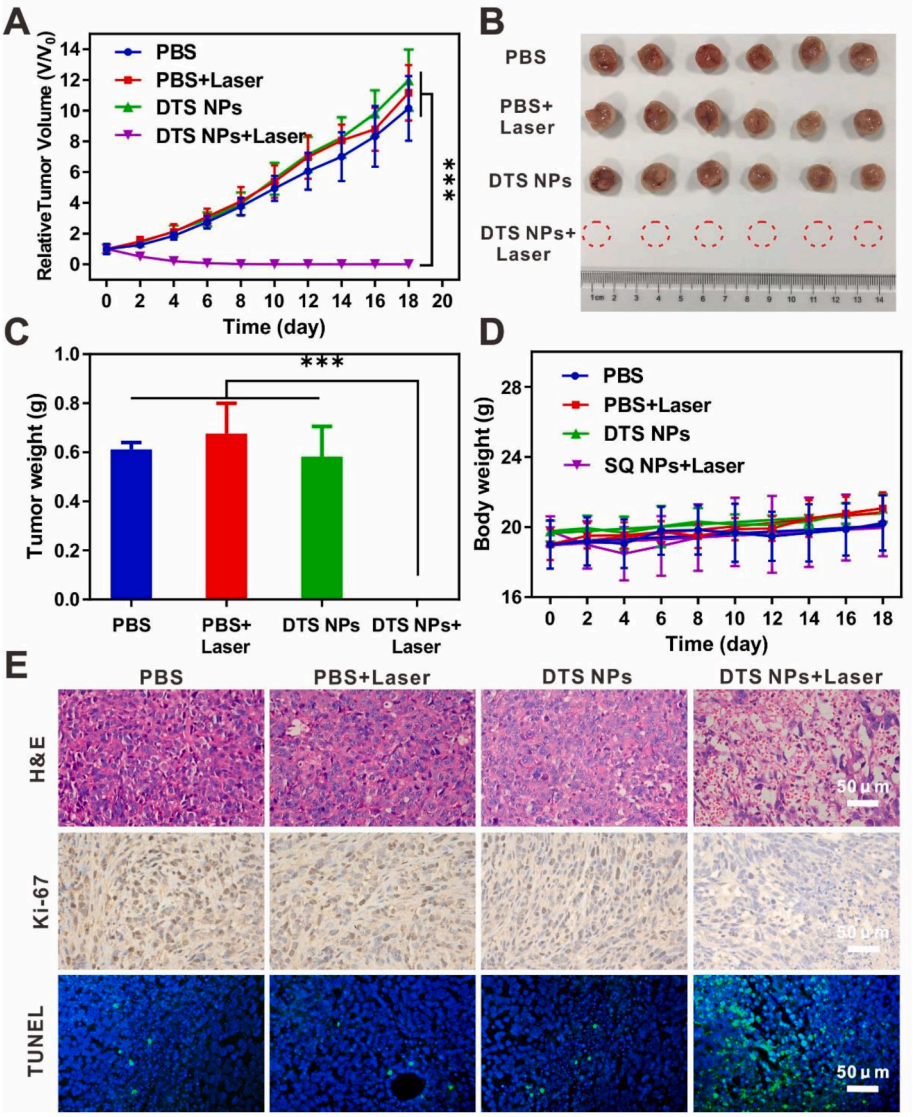

Fig. 5. A) The relative tumor volume changes of 4T1 tumor-bearing mice during treatment. B) Photograph of excised tumors from different groups after 18 days. C) The average tumor weight of various treatment groups at day 18. D) The body weight changes of mice with different treatments. E) H&E, Ki-67 and TUNEL staining analysis of tumor tissues after different treatments. Data are shown as mean ± S.D. *P < 0.05, **P < 0.01 and ***P < 0.001 were tested via a two-tailed Student's t-test.

nitrogen three times. Sequentially, 15 mL mixture of dry toluene/n-butanol (v/v, 1/1) was injected into the flask, and the reaction mixture was refluxed at 110 °C for 5 h under nitrogen atmosphere. Afterwards, the solvent was evaporated and the crude product was purified by silica-gel column chromatography by using Heane/DCM/EA (2:1:1) as eluent to give SQ-DPA-T (0.10 g) as dark green solid in 29 % yield. ^{1}H NMR (400 MHz, $CDCl_3$) δ (ppm): 7.93 (d, J = 4.7 Hz, 2H), 7.25 (d, J = 8.8 Hz, 8H), 6.91 (d, J = 8.9 Hz, 8H), 6.41 (d, J = 4.7 Hz, 2H), 3.83 (s, 12H). ^{13}C NMR (400 MHz, $CDCl_3$) δ (ppm): 178.64, 172.42, 170.35, 158.71, 147.75, 147.71, 147.18, 138.35, 137.98, 127.29, 124.56, 124.07, 119.18, 115.34, 114.58, 55.69. HRMS (*m/z*, ESI) calcd for $C_{40}H_{32}N_2O_6S_2$, 700.1702; found, 700.1686.

4.3. Single crystal X-ray crystallography

The single crystal of DTS was prepared by slowly evaporation of its dichloromethane (DCM)/n-hexane (v/v = 1:2) solution under dark surrounding, which was then subjected to single-crystal X-ray diffraction (XRD) analysis.

4.4. Preparation of DTS NPs

The nanoparticles (NPs) were prepared using one-step nano-precipitation method. Briefly, 1 mg DTS and 5 mg DSPE-PEG_{2000} was dissolved with 1 mL DMSO and then added dropwise into 8 mL deionized water on the condition of vigorous stir for 10 min. After that, the resulted dispersion was further kept in sonication for 30 min. The solution was subsequently dialyzed with deionized water for 24 h (MWCO = 3000). To prepare DiR-loaded DTS NPs, the mixture of 0.5 mg DTS, 0.5 mg DiR and 5 mg DSPE-PEG_{2000} was dissolved in 1 mL DMSO, followed by identical nanoprecipitation profile, and the hydrodynamic diameter was detected to be ~130 nm (Fig. S9).

4.5. In vitro photothermal effect

To evaluate the photothermal effect, the DTS NPs solutions were diluted to varied concentrations (0, 10, 25, and 50 μM) in centrifuge tubes and irradiated with a laser (808 nm) at various power densities (0.5, 0.8, and 1.0 W/cm^2) for 5 min. Temperature changes of DTS NPs solutions were measured by a photothermal camera. To measure the

photothermal conversion efficiency, DTS NPs NPs (50 μM) were exposed to 808 nm irradiation at 0.8 W/cm^2 for 5 min, and then the solution was cooled down to room temperature. The temperature of the solution was recorded at an interval of 30 s during this process. The photothermal conversion efficiencies (η) were measured according to the reported method:

$$\eta = \frac{hs(T_{Max} - T_{Surr}) - Q_{Dis}}{I\left(1 - 10^{-A808}\right)}$$

h is the heat transfer coefficient; s is the surface area of the container. Q_{Dis} represents heat dissipated from the laser mediated by the solvent and container. I is the laser power and A is the absorbance at 808 nm.

$$hs = \frac{mC_{water}}{\tau_s}$$

m is the mass of the solution containing the photoactive material, C is the specific heat capacity of the solution (C_{water} = 4.18 J/(g•°C), C_{DMF} = 2.14 J/(g•°C)), and τ_s is the associated time constant.

$$t = -\tau_s In\,(\theta)$$

θ is a dimensionless parameter, known as the driving force temperature.

$$\theta = \frac{T - T_{Surr}}{T_{Max} - T_{Surr}}$$

T_{Max} and T_{Surr} are the maximum steady state temperature and the environmental temperature, respectively.

4.6. Thermal- and photostability

For thermal stability, DTS NPs and ICG aqueous solution were irradiated by laser (808 nm, 0.8 W/cm^2) during five circles of heating-cooling processes. For photostability, DTS NPs and ICG aqueous solution were irradiated by laser (808 nm, 0.8 W/cm^2) for 0, 5, 10, 15, 20, 25 and 30 min, respectively. The absorbance spectrum was measured by UV–vis spectrophotometer.

4.7. In vitro cytotoxicity

The cytotoxicity toward cancer cell lines were estimated by CCK-8 assay. 4T1, CT26 and HepG2 cells were inoculated into 96-well culture plates (5×10^3 cells per well) and incubated for 24 h. Then, the cells were treated with various concentrations of DTS NPs. After incubation for 4 h, the cells were irradiated with 808 nm laser (0.8 W/cm^2) for 5 min, and another array of plates with cells were kept in the dark as the control. 24 h later, the cell counting kit-8 was added 1 h before the end of culture. The OD_{450} was measured with a 96-well plate reader and the plots of cell viability as a function of concentration of the compounds were analyzed by GraphPad Prism 7.

4.8. Live/dead cell staining assay

4T1 cells (1×10^5 cells per well) were placed into 12-well confocal plate and incubated overnight, the cells were incubated with PBS, only DTS NPs (DTS, 20 μM), only Laser (808 nm, 0.8 W/cm^2, 5 min) or DTS NPs + Laser, respectively. For the group DTS NPs + Laser, cells were incubated with 20 μM DTS NPs at 37 °C for 4 h, and followed by 808 nm laser irradiation (0.8 W/cm^2) for 5 min. After another 4 h of incubation, cells were stained with calcein-AM/PI for 30 min in darkness at 37 °C. Subsequently, the cells were gently washed and then imaged by CLSM.

4.9. Flow cytometry experiments

4T1 cells were seeded in a 12-well plate at a density of 1×10^5 cells per well and incubated for 12 h at 37 °C. After that, the 4T1 cells were incubated with PBS, only DTS NPs (DTS, 20 μM), only Laser (808 nm, 0.8 W/cm^2, 5 min) or DTS NPs + Laser, respectively. For the group DTS NPs + Laser, cells were incubated with 20 μM DTS NPs at 37 °C for 4 h, and followed by 808 nm laser irradiation (0.8 W/cm^2) for 5 min. After another 4 h of incubation, 4T1 cells treated with different formulations were collected, washed 3 times with PBS, stained with FITC-annexin V/PI apoptosis detection kit, and then measured by a flow cytometer assay.

4.10. In vivo and ex vivo NIR fluorescence

Considering that the weak fluorescence of DTS NPs itself was not suitable as a fluorescence imaging contrast agent, the commercial dye DiR and DTS were co-loaded into DSPE-PEG2000 to construct DIR-loaded DTS NPs. When the tumor volume reached 200 mm^3 by average, DiR-loaded DTS NPs (DiR, 100 μg/mL, 200 μL) were intravenously injected into the mice. At the pre-set time intervals (0, 1, 4, 8, 12, and 24 h) post injection, the mice were anesthetized and fluorescence images were taken with an IVIS Spectrum imaging system. For ex vivo fluorescence imaging, the heart, liver, spleen, lung, kidney, and tumors were dissected for imaging at 24 h post-injection.

4.11. In vitro and in vivo PA imaging

For in vitro PA imaging, DTS NPs solution at different concentrations were filled in polyethylene tubes, and then measured by a Vevo LAZR-X System. The region of interest (ROI) was presented on the images and the PA intensity values were recorded by the PA system. For in vivo PA imaging, the 4T1 tumor-bearing mice were intravenously injected with DTS NPs (DTS, 250 μg/mL, 200 μL) when the tumor volumes reached about 200 mm^3. PA images of tumor area were recorded at 0, 1, 4, 8, 12, 24 and 48 h. After data acquisition, the PA images were reconstructed using the unmixing spectra modules of PA imaging system.

4.12. In vivo photothermal imaging

When tumor volumes reached about 200 mm^3, the 4T1 tumor-bearing mice were injected (i.v.) with PBS or DTS NPs (DTS, 250 μg/mL, 200 μL). 8 h later, the tumor sites were irradiation with 808 nm laser irradiation (0.8 W/cm^2) for 10 min, and temperature variations at tumor area were recorded and imaged by using an FLIR E6390 camera.

4.13. In vivo antitumor efficacy

When the tumor volume was reached 100 mm3 on average, the mice were randomly assigned to four treatment groups (n = 6): PBS group, PBS + Laser group, DTS NPs (DTS, 250 μg/mL, 200 μL) group, and DTS NPs (DTS, 250 μg/mL, 200 μL) + Laser group. The administration was performed only once. In case of PBS + Laser and DTS NPs + Laser groups, the laser irradiation was carried out using an 808 nm laser (0.8 W/cm^2, 10 min) after post-injection for 8 h. The tumor volumes and the body weights of mice were monitored every other day for 18 d. Tumor volumes were calculated by the formula width^2 × length/2. On day 18, mice of each group were sacrificed and the tumors was excised for imaging and weighing.

4.14. Histological analyses

For PBS, PBS + Laser and DTS NPs groups, the tumors were dissected from the mice after treatment of 18 days. For the DTS NPs + Laser group, the tumors were dissected from the mice at day 2. The tumors were fixed in 10 % formalin and embedded in paraffin, and then sectioned for pathological examination including hematoxylin-eosin (H&E) staining, immunohistochemical staining for Ki-67, and terminal deoxynucleotidyl transferase dUTP nick end labeling (TUNEL). In addition, the harvested major organs from various groups were also stained by H&E to evaluate the systemic toxicity.

4.15. Statistical analysis

Quantitative results are presented as mean ± standard deviation. Statistical analysis was performed with GraphPad Prism 8.0 soft-ware. The differences between two groups were calculated by using two-tailed Student's t-test. Log-rank test for survival rates. *P < 0.05, **P < 0.01 and ***P < 0.001.

Ethics approval and consent to participate

All animal experiments were performed according to the guidelines for the care and use of laboratory animals by Shenzhen People's Hospital Animal Study Committee (approval number: AUP-240115-LZJ-0001-01).

CRediT authorship contribution statement

Xin Xie: Writing – original draft, Project administration, Funding acquisition, Conceptualization. **Yafang Dong:** Project administration, Methodology, Investigation, Data curation. **Yuan Zhang:** Methodology, Investigation. **Zongliang Xie:** Software, Methodology, Funding acquisition, Data curation. **Xinsheng Peng:** Validation, Supervision. **Yong Huang:** Visualization, Methodology, Funding acquisition. **Wei Yang:** Validation, Resources, Investigation. **Bowen Li:** Writing – review & editing, Validation, Supervision, Conceptualization. **Qiqing Zhang:** Writing – review & editing, Supervision, Funding acquisition.

Declaration of competing interest

Yuan Zhang is currently employed by Fujian Bote Biotechnology Co. Ltd. The authors declare that they have no known competing financial interests or personal relationships that could have appeared to influence the work reported in this paper.

Acknowledgements

X.X., Y.D. and Y. Z. contributed equally to this work. This work was supported by the National Natural Science Foundation of China (32101129, 52103230, 32101124), Shenzhen Basic Research Special (Natural Science Fund) basic research surface project (No. JCYJ20210324113006017), Guangdong basic and Applied Basic Research Fund Regional Joint Fund Project (key project) (No.2020B1515120091) and China Postdoctoral Science Foundation (2021M691440).

Appendix A. Supplementary data

Supplementary data to this article can be found online at https://doi.org/10.1016/j.bioactmat.2024.09.031.

References

[1] Y. Liu, P. Bhattarai, Z. Dai, X. Chen, Chem. Soc. Rev. 48 (2019) 2053.
[2] X. Li, J.F. Lovell, J. Yoon, X. Chen, Nat. Rev. Clin. Oncol. 17 (2020) 657.
[3] Y. Gao, Y. Liu, X. Li, H. Wang, Y. Yang, Y. Luo, Y. Wan, C.-s. Lee, S. Li, X.-H. Zhang, Nano-Micro Lett. 16 (2023) 21.
[4] J. Liu, T. Yang, H. Zhang, L. Weng, X. Peng, T. Liu, C. Cheng, Y. Zhang, X. Chen, Bioact. Mater. 34 (2024) 354.
[5] Y. Li, Y. Tang, W. Hu, Z. Wang, X. Li, X. Lu, S. Chen, W. Huang, Q. Fan, Adv. Sci. 10 (2023) e2204695.
[6] K. Wang, Y. Li, X. Wang, Z. Zhang, L. Cao, X. Fan, B. Wan, F. Liu, X. Zhang, Z. He, Y. Zhou, D. Wang, J. Sun, X. Chen, Nat. Commun. 14 (2023) 2950.
[7] M. Shanmugam, N. Kuthala, R. Vankayala, C.-S. Chiang, X. Kong, K.C. Hwang, ACS Nano 15 (2021) 14404.
[8] N. Choubdar, S. Avizheh, S.A. Karimifard, Curr. Drug Deliv. 19 (2022) 745.
[9] J. Guo, D. Tan, C. Lou, S. Guo, X. Jin, H. Qu, L. Jing, S. Li, Bioact. Mater. 9 (2022) 554.
[10] H.S. Jung, P. Verwilst, A. Sharma, J. Shin, J.L. Sessler, J.S. Kim, Chem. Soc. Rev. 47 (2018) 2280.
[11] S. Guo, D. Gu, Y. Yang, J. Tian, X. Chen, J. Nanobiotechnol. 21 (2023) 348.
[12] G. Chen, J. Sun, Q. Peng, Q. Sun, G. Wang, Y. Cai, X. Gu, Z. Shuai, B.Z. Tang, Adv. Mater. 32 (2020) e1908537.
[13] A. Shahrivarkevishahi, M.A. Luzuriaga, F.C. Herbert, A.C. Tumac, O.R. Brohlin, Y. H. Wijesundara, A.V. Adlooru, C. Benjamin, H. Lee, P. Parsamian, J. Gadhvi, N. J. De Nisco, J.J. Gassensmith, J. Am. Chem. Soc. 143 (2021) 16428.
[14] X. Li, L. Liu, S. Li, Y. Wan, J.-X. Chen, S. Tian, Z. Huang, Y.-F. Xiao, X. Cui, C. Xiang, Q. Tan, X.-H. Zhang, W. Guo, X.-J. Liang, C.-S. Lee, ACS Nano 13 (2019) 12901.
[15] X. Miao, W. Yao, R. Chen, M. Jia, C. Ren, H. Zhao, T. He, Q. Fan, W. Hu, Adv. Mater. 35 (2023) e2301739.
[16] X.Y. Ran, P. Chen, Y.Z. Liu, L. Shi, X. Chen, Y.H. Liu, H. Zhang, L.N. Zhang, K. Li, X. Q. Yu, Adv. Mater. 35 (2023) e2210179.
[17] J. Li, J. Wang, J. Zhang, T. Han, X. Hu, M.M.S. Lee, D. Wang, B.Z. Tang, Adv. Mater. 33 (2021) e2105999.
[18] G. Feng, G.-Q. Zhang, D. Ding, Chem. Soc. Rev. 49 (2020) 8179.
[19] A. Jablonski, Nature 131 (1933) 839.
[20] D. Wang, M.M.S. Lee, W. Xu, G. Shan, X. Zheng, R.T.K. Kwok, J.W.Y. Lam, X. Hu, B. Z. Tang, Angew. Chem. Int. Ed. 58 (2019) 5628.
[21] H. Qian, M.E. Cousins, E.H. Horak, A. Wakefield, M.D. Liptak, I. Aprahamian, Nat. Chem. 9 (2016) 83.
[22] K. Wei, Y. Wu, P. Li, X. Zheng, C. Ji, M. Yin, Nano Res. 16 (2023) 970.
[23] X. Gao, Z. Cui, Y.-R. Shen, D. Liu, Y.-J. Lin, G.-X. Jin, J. Am. Chem. Soc. 143 (2021) 17833.
[24] G. Jiang, J. Yu, J. Wang, B.Z. Tang, Aggregate 3 (2022) e285.
[25] Y.Z. Liu, X.Y. Ran, D.H. Zhou, H. Zhang, Y.J. Chen, J.X. Xu, S.Y. Chen, Q.Q. Kong, X.Q. Yu, K. Li, Adv. Funct. Mater. 34 (2024) 2311365.
[26] Z. Zhao, C. Chen, W. Wu, F. Wang, L. Du, X. Zhang, Y. Xiong, X. He, Y. Cai, R.T. K. Kwok, J.W.Y. Lam, X. Gao, P. Sun, D.L. Phillips, D. Ding, B.Z. Tang, Nat. Commun. 10 (2019) 768.
[27] D. Xi, M. Xiao, J. Cao, L. Zhao, N. Xu, S. Long, J. Fan, K. Shao, W. Sun, X. Yan, X. Peng, Adv. Mater. 32 (2020) e1907855.
[28] J. Guo, J. Dai, X. Peng, Q. Wang, S. Wang, X. Lou, F. Xia, Z. Zhao, B.Z. Tang, ACS Nano 15 (2021) 20042.
[29] S.M. Ross, J.H. Strange, J. Chem. Phys. 68 (1978) 3078.
[30] Y. Tian, D. Yin, L. Yan, WIREs Nanomed. Nanobi. 15 (2022) e1831.
[31] S. Ma, S. Du, G. Pan, S. Dai, B. Xu, W. Tian, Aggregate 2 (2021) e96.
[32] J. Sun, E. Zhao, J. Liang, H. Li, S. Zhao, G. Wang, X. Gu, B.Z. Tang, Adv. Mater. 34 (2022) e2108048.
[33] Y. Jiang, X. Zheng, Y. Deng, H. Tian, J. Ding, Z. Xie, Y. Geng, F. Wang, Angew. Chem. Int. Ed. 57 (2018) 10283.
[34] H. Shen, Y. Li, Y. Li, Aggregate 1 (2020) 57.
[35] Z. He, L. Zhao, Q. Zhang, M. Chang, C. Li, H. Zhang, Y. Lu, Y. Chen, Adv. Funct. Mater. 30 (2020) 1910301.
[36] S. Chen, Y. Pan, K. Chen, P. Chen, Q. Shen, P. Sun, W. Hu, Q. Fan, Angew. Chem. Int. Ed. 62 (2022) e202215372.
[37] S. Sengupta, F. Würthner, Acc. Chem. Res. 46 (2013) 2498.
[38] Q. Zhang, P. Yu, Y. Fan, C. Sun, H. He, X. Liu, L. Lu, M. Zhao, H. Zhang, F. Zhang, Angew. Chem. Int. Ed. 60 (2020) 3967.
[39] Y. Li, T. Ma, H. Jiang, W. Li, D. Tian, J. Zhu, Z.a. Li, Angew. Chem. Int. Ed. 61 (2022) e202203093.
[40] W. Wagner, M. Wehner, V. Stepanenko, S. Ogi, F. Würthner, Angew. Chem. Int. Ed. 56 (2017) 16008.
[41] T.E. Kaiser, V. Stepanenko, F. Würthner, J. Am. Chem. Soc. 131 (2009) 6719.
[42] T. Mirkovic, E.E. Ostroumov, J.M. Anna, R. van Grondelle, Govindjee, G. D. Scholes, Chem. Rev. 117 (2016) 249.
[43] F. Li, D. Liu, T. Wang, J. Hu, F. Meng, H. Sun, Z. Shang, P. Li, W. Feng, W. Li, X. Zhou, J. Solid State Chem. 252 (2017) 86.
[44] W. Cao, E.M. Sletten, J. Am. Chem. Soc. 140 (2018) 2727.
[45] S.L. Yefimova, G.V. Grygorova, V.K. Klochkov, I.A. Borovoy, A.V. Sorokin, Y. V. Malyukin, J. Phys. Chem. C 122 (2018) 20996.
[46] C. Sun, B. Li, M. Zhao, S. Wang, Z. Lei, L. Lu, H. Zhang, L. Feng, C. Dou, D. Yin, H. Xu, Y. Cheng, F. Zhang, J. Am. Chem. Soc. 141 (2019) 19221.
[47] M. Su, Q. Han, X. Yan, Y. Liu, P. Luo, W. Zhai, Q. Zhang, L. Li, C. Li, ACS Nano 15 (2021) 5032.
[48] S. Choi, J. Bouffard, Y. Kim, Chem. Sci. 5 (2014) 751.
[49] K. Li, X. Duan, Z. Jiang, D. Ding, Y. Chen, G.-Q. Zhang, Z. Liu, Nat. Commun. 12 (2021) 2376.
[50] X. Guo, W. Sheng, H. Pan, L. Guo, H. Zuo, Z. Wu, S. Ling, X. Jiang, Z. Chen, L. Jiao, E. Hao, Angew. Chem. Int. Ed. 63 (2024) e202319875.
[51] P. Sun, Q. Wu, X. Sun, H. Miao, W. Deng, W. Zhang, Q. Fan, W. Huang, Chem. Commun. 54 (2018) 13395.
[52] J. He, Y.J. Jo, X. Sun, W. Qiao, J. Ok, T.i. Kim, Z.a. Li, Adv. Funct. Mater. 31 (2021) 2008201.
[53] Y. Wang, G. Xia, M. Tan, M. Wang, Y. Li, H. Wang, Adv. Funct. Mater. 32 (2022) 2113098.
[54] O.P. Dimitriev, A.P. Dimitriyeva, A.I. Tolmachev, V.V. Kurdyukov, J. Phys. Chem. B 109 (2005) 4561.
[55] T. Fukuda, S. Yokomizo, S. Casa, H. Monaco, S. Manganiello, H. Wang, X. Lv, A. D. Ulumben, C. Yang, M.W. Kang, K. Inoue, M. Fukushi, T. Sumi, C. Wang, H. Kang, K. Bao, M. Henary, S. Kashiwagi, H. Soo Choi, Angew. Chem. Int. Ed. 61 (2022) e202117330.
[56] Z. Liu, T. Lu, Q. Chen, Carbon 165 (2020) 461.
[57] T. Lu, F. Chen, J. Comput. Chem. 33 (2011) 580.
[58] G. Xu, C. Li, C. Chi, L. Wu, Y. Sun, J. Zhao, X. Xia, S. Gou, Nat. Commun. 13 (2022) 3064.
[59] L. Yang, B. Huang, S. Hu, Y. An, J. Sheng, Y. Li, Y. Wang, N. Gu, Nano Res. 15 (2022) 4285.

[60] F. Würthner, T.E. Kaiser, C.R. Saha-Möller, Angew. Chem. Int. Ed. 50 (2011) 3376.
[61] J.V. Caspar, T.J. Meyer, J. Phys. Chem. 87 (2002) 952.
[62] H. Fidder, M. Rini, E.T.J. Nibbering, J. Am. Chem. Soc. 126 (2004) 3789.
[63] K. Takechi, P.V. Kamat, R.R. Avirah, K. Jyothish, D. Ramaiah, Chem. Mater. 20 (2007) 265.
[64] G. Yang, J.S. Ni, Y. Li, M. Zha, Y. Tu, K. Li, Angew. Chem. Int. Ed. 60 (2021) 5386.
[65] W. Wu, D. Mao, S. Xu, Kenry, F. Hu, X. Li, D. Kong, B. Liu, Chem 4 (2018) 1937.
[66] D. Wang, M.L. Kuzma, X. Tan, T.C. He, C. Dong, Z. Liu, J. Yang, Adv. Drug Deliv. Rev. 179 (2021) 114036.
[67] Q. Zheng, X. Liu, Y. Zheng, K.W.K. Yeung, Z. Cui, Y. Liang, Z. Li, S. Zhu, X. Wang, S. Wu, Chem. Soc. Rev. 50 (2021) 5086.
[68] X. Li, J.F. Lovell, J. Yoon, X. Chen, Nat. Rev. Clin. Oncol. 17 (2020) 657.
[69] Z. Liu, T. Lu, Q. Chen, Carbon 165 (2020) 461.
[70] T. Lu, F. Chen, J. Comput. Chem. 33 (2011) 580.
[71] A.-L. Capodilupo, V. Vergaro, G. Accorsi, E. Fabiano, F. Baldassarre, G.A. Corrente, G. Gigli, G. Ciccarella, Tetrahedron 72 (2016) 2920.